Experimental realization of deep sub-wavelength confinement of light in a topology-optimized InP nanocavity

Xiong, Meng; Christiansen, Rasmus Ellebak; Schröder, Frederik; Yu, Yi; Casses, Laura Nevenka; Semenova, Elizaveta; Yvind, Kresten; Stenger, Nicolas; Sigmund, Ole; Mørk, Jesper

Published in:
Optical Materials Express

Link to article, DOI:
10.1364/OME.513625

Publication date:
2024

Document Version
Publisher's PDF, also known as Version of record

Research Article Vol. 14, No. 2 / 1 Feb 2024 / Optical Materials Express 397
Optical Materials EXPRESS

Experimental realization of deep sub-wavelength confinement of light in a topology-optimized InP nanocavity

MENG XIONG,[1,2,*] RASMUS ELLEBÆK CHRISTIANSEN,[2,3] FREDERIK SCHRÖDER,[1,2] YI YU,[1,2] LAURA NEVENKA CASSES,[1,2] ELIZAVETA SEMENOVA,[1,2] KRESTEN YVIND,[1,2] NICOLAS STENGER,[1,2] OLE SIGMUND,[2,3] AND JESPER MØRK[1,2]

[1]*Department of Electrical and Photonics Engineering, Technical University of Denmark, Ørsteds Plads 345A, 2800 Lyngby, Denmark*
[2]*NanoPhoton - Center for Nanophotonics, Ørsteds Plads 345A, 2800 Lyngby, Denmark*
[3]*Department of Civil and Mechanical Engineering, Technical University of Denmark, Koppels Allé 404, 2800 Lyngby, Denmark*
[*]*menxi@dtu.dk*

Abstract: We experimentally demonstrate an InP nanocavity with a mode volume of 0.26 $(\lambda/2n)^3$. This is an order of magnitude smaller than the mode volumes previously demonstrated in photonic crystal point-defect cavities realized in III-V materials and four times smaller than what is often referred to as the diffraction-limited volume, $V_\lambda = (\lambda/2n)^3$. The nanocavity is designed using topology optimization, taking into account fabrication limitations, which are pushed compared to the state-of-the-art. This work thus introduces a new class of cavities featuring extreme dielectric confinement (EDC) into the realm of III-V semiconductors, offering order-of-magnitude Purcell-enhancement of the radiative rate. EDC nanocavities may thus be employed to significantly improve the properties of nanolasers, nanoLEDs and single-photon sources, among other applications.

1. Introduction

Strong spatial confinement of light in a semiconductor cavity is of significant interest for enhancing the interaction between light and matter [1], with important applications in integrated photonics [2–6] and quantum technology [7,8]. In particular, a nanocavity in which the vacuum field strength is strongly enhanced, can be used to improve the properties of light sources [4–6,9–11]. Until recently, it was held by the community that in a semiconductor, as opposed to a metal supporting plasmons, light cannot be concentrated to a mode volume smaller than $(\lambda/2n)^3$, where λ is the wavelength and n is the refractive index. This so-called "diffraction limit" was proven inapplicable by recent designs [12–15] and experimental results in silicon [16–18]. Realizing light sources using this new class of nanocavities, which we term Extreme Dielectric Confinement (EDC) nanocavities, requires implementing them in a direct-bandgap semiconductor such as III-V materials.

While the conceptual approach demonstrated for the indirect-bandgap silicon [18] can also be applied to III-V semiconductors [15], this is by no means straightforward. The processing technology for silicon benefits from decades-long optimization and refinement by the electronics industry, whereas the technology for III-V semiconductors is much less mature. In the academic world, the most common approach towards nanodevice fabrication is electron beam lithography (EBL) followed by dry etching. Even if EBL resolution is more or less the same for both Si and III-V materials, the accurate control of the etching process is much more challenging for the latter because of low etch rates and preferential loss of group-V elements, which generally lead to rough

#513625 https://doi.org/10.1364/OME.513625
Journal © 2024 Received 20 Nov 2023; revised 17 Dec 2023; accepted 18 Dec 2023; published 24 Jan 2024

Optical Materials EXPRESS

surface morphologies [19–21]. EDC nanocavities have feature sizes down to a few nanometers, which are crucial in achieving extreme light concentration [12–14] but simultaneously imply significant sensitivity towards fabrication variations [22].

Here, we experimentally demonstrate light confinement in an InP nanocavity, with characteristics approaching those achieved in silicon [18]. The light confinement is improved by more than an order of magnitude compared to photonic crystal single-point defect cavities, so-called H1-cavities [23], and is a factor of four below the "diffraction limit" of $(\lambda/2n)^3$. The spatial light confinement is experimentally demonstrated using scattering-type scanning near-field optical microscopy (s-SNOM) techniques [24–26]. Confocal cross-polarized microscopy [27] is used to demonstrate that despite the point-like spatial confinement, high quality factors can be achieved, greatly exceeding the limit of a few tens for plasmonic cavities [28–30]. The key to obtaining these results is the use of a systematic inverse design approach, taking into account the practical fabrication constraints [15,31]. In this work, we use gradient-based topology optimization [32], capable of handling large-scale inverse design problems [33], which has proven suitable for a diverse range of photonics problems [34–36] including the design of nanocavities [14,15]. Also, the refinement of the processing technology to meet the demand for nanometer-sized features is of key importance for achieving the results with high precision and performance presented. This includes especially the careful optimization of etching conditions, such as gas composition, pressure, temperature, and etching time for InP-based materials.

In this paper, two InP EDC cavity designs attained by manufacturing controlled topology optimization are presented. Electron microscope (SEM) images evidence successful fabrication of the complex cavity designs. The cavity quality factor is measured using confocal cross-polarized microscopy and the optical near-field amplitude is extracted from s-SNOM measurements. The experimental results show good agreement with simulation results, confirming the demonstration of a III-V semiconductor nanocavity achieving light confinement deep below the diffraction volume $V_\lambda = (\lambda/2n)^3$. We also investigate the implications of breaking the fabrication constraints, e.g., allowing for non-vertical sidewalls in the membrane structures, which shows that additional improvement of the light confinement is possible by 3D-shaping the structures.

2. Design and fabrication

The cavity geometries achieving extreme dielectric confinement have as their central feature a bowtie-like structure, which acts to spatially confine light by exploiting the boundary conditions of Maxwell's equations for the electromagnetic field [12–14,23,37]. In order to achieve strong light confinement, the feature sizes of the central part of the bowtie, i.e., the bridge width and curvature, need to be in the range of a few nanometers [38]. To obtain an optimal design, it is important to take into account the constraints of the fabrication process to be used [18]. To do so, we first design a cavity with extreme dielectric confinement using topology-optimization (TO-EDC cavities) with relaxed geometric constraints. Next, we fabricate the structure in InP and test the nanofabrication accuracy. The fabrication accuracy is found to be limited by EBL and dry etching. After the first round of fabrication optimization, we achieved the smallest dielectric feature size of 20 nm. The smallest feature size has a variation of ±10 nm, depending on the design of the bowtie nanostructure, and originates from the limited resolution of the dry etching. The proximity effect also results in shape deformation of the air voids. Subsequently, minimum dielectric feature sizes of 20 nm and 15 nm for two separate design runs are set as the geometrical constraints for the second round of topological optimization. In addition, a minimum curvature with a radius of 25 nm is imposed for sharp corners of the air void regions.

The photonic cavity designs that optimize the ratio Q/V between the cavity quality factor Q and the optical mode volume V, are generated using topology optimization based on the finite-element method (FEM) [39] and employing a local density of states approach [40]. In brief, the problem of designing the cavities is formulated as a constrained, continuous, mathematical

Optical Materials EXPRESS

optimization problem, which is solved using the method of moving asymptotes [41] employing adjoint sensitivity analysis [42] for efficient gradient calculations. The design variables to be optimized describe the distribution of the material constituting the photonic cavity through an interpolated refractive index [43]. The initial guess used for the design variables corresponds to a non-physical mixture of 50% air and 50% InP at every point in the design domain. This initial material distribution is gradually changed by solving the optimization problem using ~1000 design iterations while employing a standard filtering and threshold continuation approach to ensure a final physically realizable design [44,45]. The prescribed material length scales are ensured through a set of constraints imposed on the optimization problem [31]. Once an optimized geometry has been reached, the final material distribution is carefully extracted and curve fitted for post-evaluation in a second round of simulations using high-resolution models. The membrane thickness of the structure is fixed at 245 nm during the optimization.

In all cases, we find that the final structure develops a central bowtie feature, as also found in [18]. The width of the central bowtie bridge is an important characteristic of a given design since it, to a large extent, dictates the degree of spatial light concentration possible in the structure [18]. We here focus on two designs with prescribed bowtie bridge widths (g) of 15 nm and 20 nm, henceforth denoted TO-EDC g15 and TO-EDC g20. Two numerical approaches, 3D finite difference time domain (FDTD) method and 3D FEM, were used for the second round of simulations. Figure 1(a) shows the TO-EDC g20 design, with the grey and black areas representing the dielectric and air regions, respectively. Simulations of the cavity mode field, in this case, based on the FDTD, are shown in Figs. 1(b) and (c), illustrating that the electrical field of the EDC mode is indeed strongly confined within the central dielectric bridge of the bowtie nanostructure. Simulations of the resulting structures show that the EDC mode has a resonant wavelength of 1539.7 nm with a Q-factor of ~1000 and a mode volume of 0.26 $(\lambda/2n)^3$, which is significantly below the diffraction volume $V_\lambda = (\lambda/2n)^3$ and a factor of 1/13 of the mode volume of a point-defect cavity (of H1 type [23]). The mode volume is calculated as the spatial integral of the electric field divided by the field strength at the position of interest. We emphasize that the mode volume depends on the position, which is here taken at the center of the bowtie bridge, with the inverse of the mode volume being a measure of the vacuum field strength at that position [46].

As the bridge width g is further reduced to 15 nm (TO-EDC g15), the mode volume reduces to 0.19 $(\lambda/2n)^3$. Such a reduction of the mode volume is also accompanied by a Q-factor reduction. However, the calculated Q-factor drops only 20% to 800 (with a resonant wavelength slightly shifted to 1538.4 nm), leading to an increased Q/V of 4210 $(\lambda/2n)^{-3}$ for TO-EDC g15, as compared with a Q/V of 3840 $(\lambda/2n)^{-3}$ for TO-EDC g20. It is noted that not only the central bridge width changes between the two optimized designs, but also the size and shape of the air-holes throughout the cavity changes, with differences of up to 20 nm and 180 nm for the inner and outermost regions, respectively. These results imply that one needs to carefully design the entire device geometry to ensure the best possible performance, not only change the size of individual features.

Compared to earlier topology-optimized designs [15,18], the design in Fig. 1(a) is free from the many fine features (hair-like extrusions) mainly due to length scale constraints. Recent work also showed that a simpler cavity design, limited to the combination of elementary geometric shapes, can perform nearly as well as the full topology-optimized structure, allowing adaptation of the design to other wavelengths and membrane dimensions [22].

We fabricated the cavities in a 245 nm thick InP membrane, which was bonded to a Si/SiO_2 substrate. The Si/SiO_2 substrate was prepared through oxidation and annealing of a Si wafer in an anneal-oxide furnace at 1100 degrees Celsius, yielding a SiO_2 layer with a thickness of 2.7 µm. This SiO_2 layer serves as a sacrificial layer for the membranization of the devices. A 245-nm-thick layer of InP, accompanied by a 100 nm-thick InGaAs etch-stop layer was grown on an InP substrate via metal-organic vapor phase epitaxy (MOVPE). Before bonding, the surfaces

Optical Materials EXPRESS

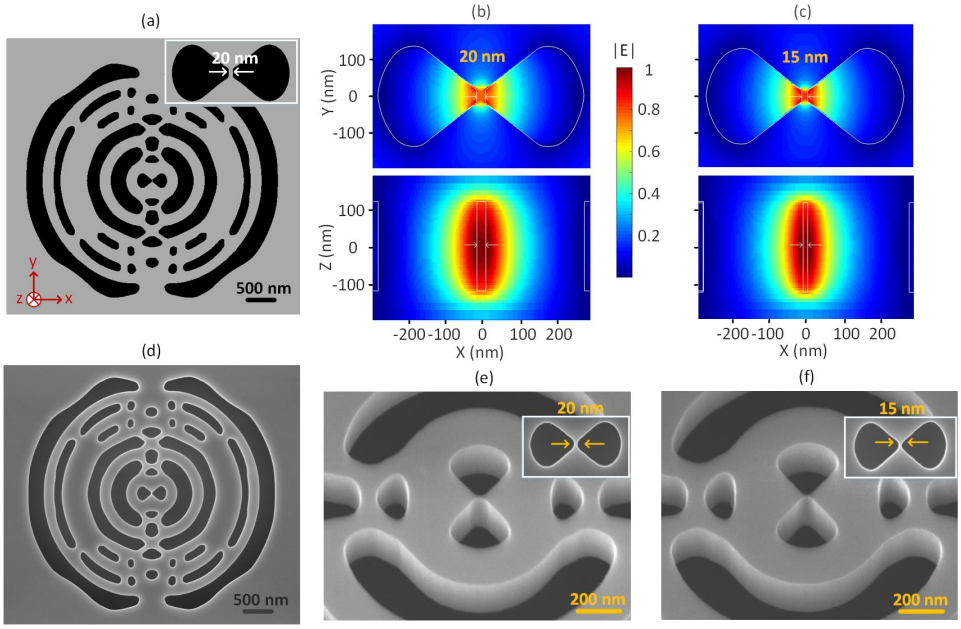

Fig. 1. (a) Design of the TO-EDC g20 cavity, with the smallest dielectric feature size (corresponding to the dielectric bridge width at the center) of 20 nm. The grey and black areas represent the dielectric and air void regions. The inset shows a zoom-in of the central bridge of the cavity. (b, c) Calculated electric field distribution ($|E|$) in the XY plane (top, Z = 0) and XZ cross-section (bottom, Y = 0) of the target cavity mode at the center (500 nm by 400 nm) of the (b) TO-EDC g20 and (c) TO-EDC g15, respectively. (d) SEM image (top view) of the fabricated TO-EDC g20 based on InP. (e, f) SEM images of the tilted views of the central areas of the (e) TO-EDC g20 and (f) TO-EDC g15, respectively. The insets in (e) and (f) are top views of the central bridges of the respective cavities.

of both the InP wafer and Si/SiO_2 substrate were activated using O_2 plasma for 30 seconds. Subsequently, the InP wafer was directly bonded to the Si/SiO_2 substrate under a force of 2 kN in Süss SB6 wafer bonder at 300 degrees Celsius. After removing the InP substrate and InGaAs etch-stop layer, the InP membrane for the cavity was formed.

We deposited a layer of 100 nm SiNx onto the wafer, and subsequently spin-coated a layer of 180 nm chemically semi-amplified resist (CSAR6200.09) on top. The SiNx and CSAR were used as a hard mask and photoresist, respectively. The thicknesses of these masks were optimized to strike a balance—ensuring they were sufficiently thin to enable the etchant to access the narrow cavity opening, yet not overly thin to compromise the protection of the underlying materials.

The cavity structures were exposed on JEOL-9500FSZ electron-beam writer with current I = 0.2 nA and shot pitch of 1 nm. The low current and fine shot pitch were chosen to achieve high resolution. The pattern was transferred to the SiNx hard mask and InP layer by a two-step inductively coupled plasma (ICP) etching. The sample was put on a Si wafer in ICP. The presence of the Si wafer served as a passivation layer that could accumulate on the sidewalls, mitigating lateral etching [21]. For the InP etching process, HBr gas was employed with a controlled flow rate of 5 sccm. This deliberate choice of a low gas flow rate was important in achieving a low pressure of 0.5 mTorr. This reduction in pressure played a crucial role in the formation of straight sidewalls in the etched structures. After the etching, a buffered HF wet etching is applied to membranize the structures.

Optical Materials EXPRESS

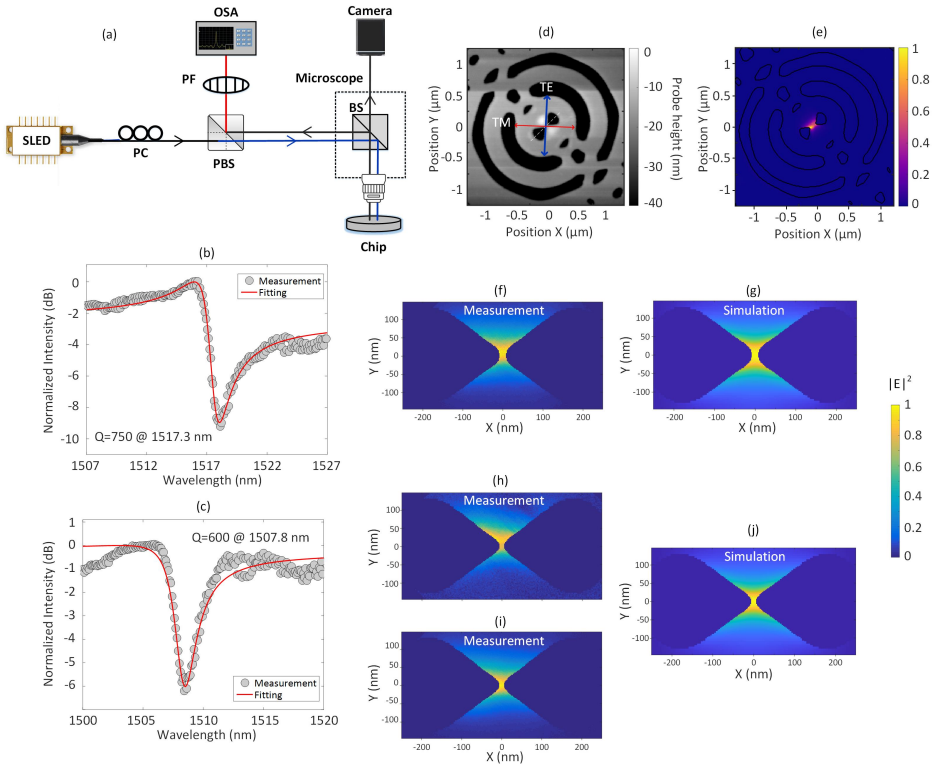

Fig. 2. (a) Confocal cross-polarized microscopy setup used to measure the quality factor of the structures. The TE component (blue line) of the pump light (black line) generated by a superluminescent diode (SLED) is selected by a polarization beam splitter (PBS) and then focused onto the surface of the sample through a microscope objective. (b, c) Measured scattering spectra (grey circles) and the corresponding theoretical fits (red curves) of the (b) TO-EDC g20 and (c) TO-EDC g15, respectively. (d) Topography and (e) near-field amplitude signal at the resonant frequency of the TO-EDC g20 cavity, as measured by an AFM-based s-SNOM. (f-g) Normalized amplitudes of (f) the measured scattered light from the cavity center and (g) the calculated field intensity of TO-EDC g20. (h, i) Normalized amplitudes of the measured scattered light from the cavity center of TO-EDC g15 with a sacrificial layer of (h) 2 μm and (i) 1.1 μm, respectively. (j) the calculated field intensity of TO-EDC g15. The data in the air voids is disregarded.

Figures 1(d-f) shows SEM images of the fabricated samples. Instead of the designed wedge-shaped dielectric bridge for the bowtie nanostructure, the fabricated structure is, to some extent, rounded at the bowtie tip due to the limited resolution of the EBL and the following development.

3. Experimental results

To measure the Q-factor of the TO-EDC cavities, we use a cross-polarized confocal setup, cf. Figure 2(a). The TE component (blue line) of the pump light (black line) generated by a superluminescent diode (SLED) with a broadband emission ranging from 1460 to 1620 nm is selected by a polarization beam splitter (PBS) and then focused onto the surface of the sample through a microscope objective. The light excites the EDC mode, which contains both TE and TM components (defined as in Fig. 2(d)). The TM component of the scattered light (red line), together with the light from the InP membrane, is then reflected by the same PBS and measured

Optical Materials EXPRESS

by an optical spectrum analyzer (OSA), while the TE-polarized light is filtered out by the PBS. The TE and TM components are both at a 45-degree to the bridge direction of the cavity, as shown in Fig. 2(d).

Asymmetric Fano lineshapes are observed in the scattering spectra (grey circles) (Figs. 2(b, c)) due to field interference between the scattered light from the excited EDC mode (a discrete mode) and the light scattered directly from the InP membrane (a continuum of modes). To investigate other causes of the asymmetric lineshapes, we have conducted experiments where we systematically varied the pump power and analyzed the corresponding light scattering spectra. Our findings indicate that the lineshape asymmetry is independent of the power level. This observation leads us to conclude that the asymmetry is unlikely to be induced by nonlinear effects inherent to InP. Nonlinear effects – namely, free-carrier excitation induced by two-photon absorption (which typically results in a blue shift of the resonance) and thermal nonlinearity (leading to a red shift) – might effectively counterbalance each other. This compensation could conceal any significant deformation in the resonance lineshape under CW pumping that would otherwise be observable, but the moderate Q-factor of the cavity makes this unlikely. The simple Fano formula can describe such a scattering spectrum

$$|R(\omega)|^2 = \left| \frac{\gamma_v}{j(\omega_0 - \omega) + \gamma_T} + |r_B| e^{j\theta} \right|^2 \tag{1}$$

where ω is the frequency of the input light and ω_0 is the resonant frequency of the EDC mode. Here, $\gamma_v = \omega_0 / 2Q_v$ and $\gamma_T = \omega_0 / 2Q_T$ are the field decay rates of the EDC mode, in which Q_v and Q_T are the intrinsic (without fabrication imperfection and material absorption) and total (with fabrication imperfection and material absorption) Q-factors of the EDC mode, respectively. Also, $|r_B|$ is the field reflectivity of the InP membrane and $e^{j\theta}$ is a propagation factor in which θ is the phase difference between the localized EDC mode and the background continuum mode. Such a phase shift can be controlled by adjusting the focus of the objective lens.

Equation (1) is used to fit the measurements (Figs. 2(b) and (c)), resulting in Q-factors of TO-EDC g15 and TO-EDC g20, respectively. The measured Q-factors of the fabricated cavities are found to be reduced by about 25% compared to the simulated values for the nominal designs. This reduction most probably originates from fabrication imperfections, including geometric perturbations and sidewall roughness. Compared with the design, the resonant wavelength of the TO-EDC g20 (g15) blue shifts by 22 (32) nm due to the non-straight etching profile, which will be further explained in the next section. The larger shift for the TO-EDC g15 is consistent with a smaller bowtie gap associated with a stronger mode localization, which is more sensitive to fabrication errors [22].

The ultra-small mode volume of EDC cavities makes the experimental characterization of the EDC mode challenging. We exploit s-SNOM for characterizing the spatial field distribution of the cavity mode [18,24]. The s-SNOM contains an AFM operating in tapping mode [47]. A tunable CW laser is focused on the tip apex with a nominal radius of 20 nm and an effective distance of 5 nm from the sample surface. Therefore, the light is scattered 25 nm above the sample surface [24]. The CW laser is s-polarized and aligned with the cavity mode to minimize the excitation of the tip [48] and maximize the excitation of the cavity. The scattered light is detected with a photodiode and a linear polarizer, ensuring detection in s-polarization [49,50]. Demodulation at higher harmonics of the tip tapping frequency Ω [25,26] and using a pseudo-heterodyne interferometric detection scheme [51] allows retrieval of the near-field amplitude with a spatial resolution of the order of the tip radius. We present the data retrieved from the fourth harmonic. Scanning the sample below the AFM tip allows to retrieve the spatial field distribution of the near-field amplitude. Figures 2(d) and (e) show the measured AFM topography of the TO-EDC g20 and the corresponding optical near-field signal of the EDC mode. Compared to the SEM image in Fig. 1(d), the cavity topography measured by the AFM is a bit distorted due to the

Optical Materials EXPRESS

limited resolution of the AFM as the tip goes down into the air voids of the structure. Indeed, the EDC mode is strongly confined at the bowtie center, whereas the enhanced fields at the bowtie edge arise due to the combination of the surface field and the field in the void [18].

We compare the experimental data with simulation results. We disregard the data in the air void regions, since, in these regions, the tip goes down into the holes and a complex combination of surface fields and the field in the voids is measured. See [18] for an extensive discussion. Figures 2(f) and (g), respectively, show the normalized amplitudes of the measured scattered light $|E_m|$ and the calculated field intensity $|E_c|$ of the EDC mode at the cavity center about 25 nm above the surface.

The Bhattacharyya coefficient $t = \sum \sqrt{|E_m|\,|E_c|}$ is used to evaluate the similarity between the measured and calculated field intensities, where both fields are normalized as $\sum |E_m| = \sum |E_c| = 1$. A larger value of t (closer to 1) means a better agreement between the measurement and the simulation. This calculation yields $t = 0.97$ for the cavity TO-EDC g20. As seen, the measured and calculated field profiles (Figs. 2(f) and (g)) are almost identical, except that the measured profile is a bit asymmetric with respect to the x and y axes. This may be caused by instabilities due to mechanical or thermal expansion of the InP membrane during the AFM scanning. In addition, heating up the system while focusing the laser on the tip and on the bowtie alters the refractive index of InP, thus shifting the cavity mode while scanning. Such an asymmetry becomes more pronounced when the bowtie gap shrinks to 15 nm, as shown in Fig. 2(h), where the Bhattacharyya coefficient t reduces slightly to 0.9584 which is a bit lower than that of TO-EDC g20. This suggests that the near-field measurement becomes more sensitive to instability issues when light is further confined.

Interestingly, we found such an instability issue can be relieved by decreasing the sacrificial layer (the SiO_2 layer) beneath the InP membrane. As seen from Fig. 2(i), the measured scattered light from another TO-EDC g15 but with a thinner (1.1 μm) sacrificial layer shows improved stability and, thus, less asymmetry in the mode profile. This is confirmed by comparing with the calculated field intensity (Fig. 2(j)), where the Bhattacharyya coefficient t reaches the maximum of 0.9761.

4. Exploration of fabrication limits

In order to further investigate the fabrication limits, we reduce the bridge width of the bowtie gap of TO-EDC g20 (going below 20 nm) while keeping the rest of the structural parameters unchanged. Here, a sacrificial layer of 1.1 μm is used to alleviate the instability issue.

Figure 3(a) shows that a dielectric bridge as narrow as 10 nm can be achieved, albeit with a small upper part of the bridge being etched away. When the targeted bowtie bridge width is further reduced to 8 nm, the upper part of the bridge is further etched, with the air groove now reaching down to the central plane of the membrane, cf. Figure 3(b). This also implies that the etching profile is not straight through the InP membrane and indicates that the bridge width in the central plane in the nominal 10 nm case (Fig. 3(a)) is less than 10 nm.

We then measure the s-SNOM signal for the new TO-EDC g20 cavity with the 10 nm gap (Fig. 3(d)). Compared to the original TO-EDC g20 and TO-EDC g15 cavities, the new cavity displays even stronger light confinement. The measured scattered mode intensity (Fig. 3(e)) agrees well with the calculated one (Fig. 3(f)), as shown by an overlap coefficient t of 0.9546. It should be noted that in the bowtie center, we use the calculated field about 30 nm under the cavity surface due to the loss of the upper InP. This comparison becomes more reasonable if we take into account the influence of the AFM probe tip. Figure 3(g) shows the convolution of the simulated electric field $|E_s|$ of the EDC mode and the AFM probe function $f(\delta)$, which is treated here as a two-dimensional Gaussian distribution with a standard deviation of δ. By sweeping the value of δ, the maximum value of $t = 0.9868$ is found when $\delta = 10$ nm.

Optical Materials EXPRESS

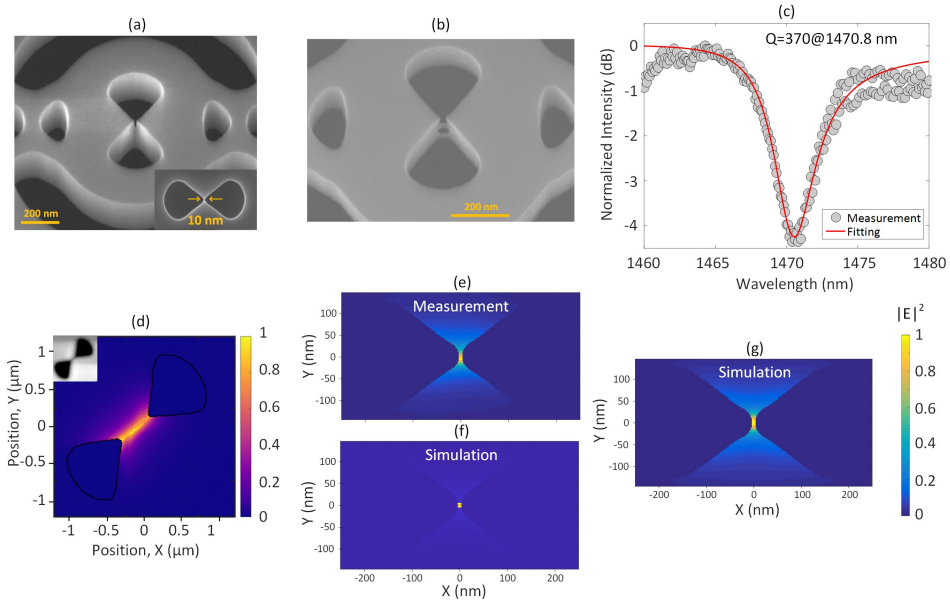

Fig. 3. (a) SEM image showing a tilted view of the central area of the modified TO-EDC g20 cavity with a 10 nm gap. The inset shows the top view of the central bridge. (b) SEM image showing the tilted view of the central area of the modified TO-EDC g20 cavity with an 8 nm gap. (c) Measured scattering spectra (grey circles) and the corresponding theoretical fits (red line) of the modified TO-EDC cavity g20 with a 10 nm dielectric gap. (d) Measured near-field amplitude signal at the cavity resonant frequency. The inset shows the topography of the central region as obtained from AFM measurements. (e) Normalized amplitudes of the measured scattered light at the cavity center. (f, g) The calculated field intensity at the cavity center (f) with and (g) without convolution with the AFM probe function. The data in the air voids is disregarded.

From the simulations, we infer a mode volume of 0.16 $(\lambda/2n)^3$. From the scattering spectra, we obtain a Q-factor of 370, which is reduced from a value of 475 expected from the simulations. The resonance frequency is also observed to exhibit a large blue shift. Both features are consistent with a non-straight etching profile, which leads to additional scattering and a larger fraction of the EDC mode residing in air rather than within the solid material of the cavity. The presence of a greater fraction of the EDC mode in air alters the effective refractive index experienced by the mode, leading to a blue shift of the resonance.

We also perform FDTD simulations on structures with angled etching profiles of the central dielectric bridge. We find that the corresponding mode volume can be as small as 0.12 $(\lambda/2n)^3$ when the bridge width in the central plane of the InP membrane reduces to 4 nm. The reduction in bridge width leads to the decrease in the mode volume. Additionally, non-straight and non-uniform etching profiles enhance light confinement in the vertical direction, so it may thus be used to further shrink the mode volume. The approach is probably not practical, though, since the fabrication process will be difficult to control. A better approach will be to replace the SiNx with a harder mask and systematically reduce the bridge width through process optimization. Compared to the Si cavity in [18], the InP cavity here has a larger mode volume, despite its a narrower bridge width. This difference can be attributed to two factors: First, Si has a higher refractive index than InP, which enhances light confinement in Si. Second, the cavity was obtained by altering the design of TO-EDC g20, which means that the Q/V ratio is not optimized.

Optical Materials EXPRESS

It is worth noting that the mode volume can be potentially reduced to as small as 0.075 $(\lambda/2n)^3$ by a new round of topology optimization.

5. Conclusions

We have demonstrated an InP nanocavity with an optical mode volume of 0.26 $(\lambda/2n)^3$, which is more than an order of magnitude smaller than what was previously observed in III-V semiconductor nanocavities. The cavity was designed using topology optimization taking into account fabrication constraints. This class of EDC (Extreme Dielectric Confinement) cavities confines light in the semiconductor material rather than in air and can be used to enhance the radiative rate of band-to-band transitions within the semiconductor. It thus holds promise for realizing nanolasers and nanoLEDs with ultra-small active region or single-photon sources with enhanced emission rates. Further reduction of the mode volume can be achieved by improving the fabrication accuracy.

Funding. Danmarks Grundforskningsfond (DNRF147, NanoPhoton); European Research Council (834410, FANO).

Disclosures. The authors declare no conflicts of interest.

Data availability. Data underlying the results presented in this paper may be obtained from the authors upon reasonable request.

References

1. Y. Akahane, T. Asano, B.-S. Song, *et al.*, "High-Q photonic nanocavity in a two-dimensional photonic crystal," Nature **425**(6961), 944–947 (2003).
2. K. Nozaki, S. Matsuo, T. Fujii, *et al.*, "Femtofarad optoelectronic integration demonstrating energy-saving signal conversion and nonlinear functions," Nat. Photonics **13**(7), 454–459 (2019).
3. O. Painter, R. K. Lee, A. Scherer, *et al.*, "Two-dimensional photonic band-gap defect mode laser," Science **284**(5421), 1819–1821 (1999).
4. S. Matsuo, A. Shinya, T. Kakitsuka, *et al.*, "High-speed ultracompact buried heterostructure photonic-crystal laser with 13 fJ of energy consumed per bit transmitted," Nat. Photonics **4**(9), 648–654 (2010).
5. G. Crosnier, D. Sanchez, S. Bouchoule, *et al.*, "Hybrid indium phosphide-on-silicon nanolaser diode," Nat. Photonics **11**(5), 297–300 (2017).
6. E. Dimopoulos, M. Xiong, A. Sakanas, *et al.*, "Experimental demonstration of nanolaser with sub-μA threshold current," Optica **10**(8), 973–976 (2023).
7. J. P. Reithmaier, G. Sęk, A. Löffler, *et al.*, "Strong coupling in a single quantum dot-semiconductor microcavity system," Nature **432**(7014), 197–200 (2004).
8. T. G. Tiecke, J. D. Thompson, N. P. De Leon, *et al.*, "Nanophotonic quantum phase switch with a single atom," Nature **508**(7495), 241–244 (2014).
9. S. Nakayama, S. Ishida, S. Iwamoto, *et al.*, "Effect of cavity mode volume on photoluminescence from silicon photonic crystal nanocavities," Appl. Phys. Lett. **98**(17), 171102 (2011).
10. J. Mork and K. Yvind, "Squeezing of intensity noise in nanolasers and nanoLEDs with extreme dielectric confinement," Optica **7**(11), 1641–1644 (2020).
11. M. Saldutti, Y. Yu, and J. Mørk, "The threshold of semiconductor nanolasers," arXiv, arXiv:2305.15888 (2023).
12. J. T. Robinson, C. Manolatou, L. Chen, *et al.*, "Ultrasmall mode volumes in dielectric optical microcavities," Phys. Rev. Lett. **95**(14), 143901 (2005).
13. S. Hu and S. M. Weiss, "Design of photonic crystal cavities for extreme light concentration," ACS Photonics **3**(9), 1647–1653 (2016).
14. H. Choi, M. Heuck, and D. Englund, "Self-similar nanocavity design with ultrasmall mode volume for single-photon nonlinearities," Phys. Rev. Lett. **118**(22), 223605 (2017).
15. F. Wang, R. E. Christiansen, Y. Yu, *et al.*, "Maximizing the quality factor to mode volume ratio for ultra-small photonic crystal cavities," Appl. Phys. Lett. **113**(24), 241101 (2018).
16. S. Hu, M. Khater, R. Salas-Montiel, *et al.*, "Experimental realization of deep-subwavelength confinement in dielectric optical resonators_SI," Sci. Adv. **4**(8), eaat2355 (2018).
17. J. Zhou, J. Zheng, Z. Fang, *et al.*, "Ultra-low mode volume on-substrate silicon nanobeam cavity," Opt. Express **27**(21), 30692 (2019).
18. M. Albrechtsen, B. Vosoughi Lahijani, R. E. Christiansen, *et al.*, "Nanometer-scale photon confinement in topology-optimized dielectric cavities," Nat. Commun. **13**(1), 6281 (2022).
19. T. R. Hayes, "Reactive ion etching of InP using CH4/H2 mixtures: Mechanisms of etching and anisotropy," J. Vac. Sci. Technol., B: Microelectron. Process. Phenom. **7**(5), 1130–1140 (1989).

Optical Materials EXPRESS

20. S. Bouchoule, G. Patriarche, S. Guilet, *et al.*, "Sidewall passivation assisted by a silicon coverplate during Cl2–H2 and HBr inductively coupled plasma etching of InP for photonic devices," J. Vac. Sci. Technol., B: Microelectron. Nanometer Struct.–Process., Meas., Phenom. **26**(2), 666–674 (2008).
21. S. Bouchoule, S. Azouigui, S. Guilet, *et al.*, "Anisotropic and smooth inductively coupled plasma etching of III-V laser waveguides using HBr-O2 chemistry," J. Electrochem. Soc. **155**(10), H778–H785 (2008).
22. G. Kountouris, J. Mørk, E. V. Denning, *et al.*, "Modal properties of dielectric bowtie cavities with deep sub-wavelength confinement," Opt. Express **30**(22), 40367–40378 (2022).
23. M. Saldutti, M. Xiong, E. Dimopoulos, *et al.*, "Modal properties of photonic crystal cavities and applications to lasers," Nanomaterials **11**(11), 3030 (2021).
24. B. Knoll and F. Keilmann, "Enhanced dielectric contrast in scattering-type scanning near-field optical microscopy," Opt. Commun. **182**(4-6), 321–328 (2000).
25. M. B. Raschke and C. Lienau, "Apertureless near-field optical microscopy: Tip–sample coupling in elastic light scattering," Appl. Phys. Lett. **83**(24), 5089–5091 (2003).
26. J. M. Atkin, S. Berweger, A. C. Jones, *et al.*, "Nano-optical imaging and spectroscopy of order, phases, and domains in complex solids," Adv. Phys. **61**(6), 745–842 (2012).
27. M. Galli, S. L. Portalupi, M. Belotti, *et al.*, "Light scattering and fano resonances in high-Q photonic crystal nanocavities," Appl. Phys. Lett. **94**(7), 071101 (2009).
28. F. Wang and Y. R. Shen, "General properties of local plasmons in metal nanostructures," Phys. Rev. Lett. **97**(20), 206806 (2006).
29. G. V. Naik, V. M. Shalaev, and A. Boltasseva, "Alternative plasmonic materials: Beyond gold and silver," Adv. Mater. **25**(24), 3264–3294 (2013).
30. J. B. Khurgin, "How to deal with the loss in plasmonics and metamaterials," Nat. Nanotechnol. **10**(1), 2–6 (2015).
31. M. Zhou, B. S. Lazarov, F. Wang, *et al.*, "Minimum length scale in topology optimization by geometric constraints," Comput. Methods Appl. Mech. Eng. **293**, 266–282 (2015).
32. M. P. Bendsøe and O. Sigmund, *Topology Optimization* (Springer Berlin, Heidelberg, 2004).
33. N. Aage, E. Andreassen, B. S. Lazarov, *et al.*, "Giga-voxel computational morphogenesis for structural design," Nature **550**(7674), 84–86 (2017).
34. J. S. Jensen and O. Sigmund, "Topology optimization for nano-photonics," Laser Photonics Rev. **5**(2), 308–321 (2011).
35. S. Molesky, Z. Lin, A. Y. Piggott, *et al.*, "Inverse design in nanophotonics," Nat. Photonics **12**(11), 659–670 (2018).
36. R. E. Christiansen and O. Sigmund, "Inverse design in photonics by topology optimization: tutorial," J. Opt. Soc. Am. B **38**(2), 496–509 (2021).
37. S. Mignuzzi, S. Vezzoli, S. A. R. Horsley, *et al.*, "Nanoscale Design of the Local Density of Optical States," Nano Lett. **19**(3), 1613–1617 (2019).
38. M. Albrechtsen, B. Vosoughi Lahijani, and S. Stobbe, "Two regimes of confinement in photonic nanocavities: bulk confinement versus lightning rods," Opt. Express **30**(9), 15458–15469 (2022).
39. J. Jin, *The Finite Element Method in Electromagnetics*, 3rd Edition (Wiley-IEEE Press, 2014).
40. X. Liang and S. G. Johnson, "Formulation for scalable optimization of microcavities via the frequency-averaged local density of states," Opt. Express **21**(25), 30812–30841 (2013).
41. K. Svanberg, "A class of globally convergent optimization methods based on conservative convex separable approximations," SIAM J. Optim. **12**(2), 555–573 (2002).
42. D. A. Tortorelli and P. Michaleris, "Design sensitivity analysis: Overview and review," Inverse Probl. Eng. **1**(1), 71–105 (1994).
43. R. E. Christiansen, J. Vester-Petersen, S. P. Madsen, *et al.*, "A non-linear material interpolation for design of metallic nano-particles using topology optimization," Comput. Methods Appl. Mech. Eng. **343**, 23–39 (2019).
44. B. Bourdin, "Filters in topology optimization," Int. J. Numer. Methods Eng. **50**(9), 2143–2158 (2001).
45. F. Wang, B. S. Lazarov, and O. Sigmund, "On projection methods, convergence and robust formulations in topology optimization," Struct. Multidiscip. Optim. **43**(6), 767–784 (2011).
46. P. T. Kristensen, C. Van Vlack, and S. Hughes, "Effective mode volumes for leaky optical cavities," AIP Conf. Proc. **1398**, 100–102 (2011).
47. L. N. Casses, K. J. Kaltenecker, S. Xiao, *et al.*, "Quantitative near-field characterization of surface plasmon polaritons on monocrystalline gold platelets," Opt. Express **30**(7), 11181–11191 (2022).
48. L. Novotny and B. Hecht, *Principles of Nano-Optics*, 2nd Edition (Cambridge University Press, 2012).
49. M. Schnell, A. Garcia-Etxarri, J. Alkorta, *et al.*, "Phase-resolved mapping of the near-field vector and polarization state in nanoscale antenna gaps," Nano Lett. **10**(9), 3524–3528 (2010).
50. Z. H. Kim and S. R. Leone, "Polarization-selective mapping of near-field intensity and phase around gold nanoparticles using apertureless near-field microscopy," Opt. Express **16**(3), 1733–1741 (2008).
51. N. Ocelic, A. Huber, and R. Hillenbrand, "Pseudoheterodyne detection for background-free near-field spectroscopy," Appl. Phys. Lett. **89**(10), 8–11 (2006).